

CFD-Aerosol Modeling of the Effects of Wall Composition and Inlet Conditions on Carbon Nanotube Catalyst Particle Activity

David P. Brown^{1,2,*}, Albert G. Nasibulin¹, and Esko I. Kauppinen¹

¹Helsinki University of Technology, Center for New Materials and Department of Engineering Physics and Mathematics, Puumiehenkuja 2, Espoo, P.O. Box 5100, FIN-02150, Finland; and

²StreamWise, 5860 Leeland St. S., St. Petersburg, Florida, 33715, USA

The evolution of iron catalyst particles during aerosol (floating catalyst) Chemical Vapor Deposition (CVD) synthesis of Carbon Nanotubes (CNTs) from CO is computed using a multi species Computational Fluid Dynamics (CFD) model incorporating a lognormal aerosol method of moments (MOM) to describe their dynamics and a combined chemical kinetics and equilibrium model for catalytic production of CO₂. The influence of the presence of iron at the reactor walls, the fed particle size, number concentration and polydispersity and the effect of the catalytic production of CO₂ at the reactor wall are studied in terms of particle size, concentration and polydispersity and reagent concentration during CNT synthesis. It is found that iron catalyst particle dynamics are essentially insensitive to wall iron concentrations and, for a wide range of particle sizes and concentrations, it is found that the catalyst particles are stable up to a critical CNT window in which CNT nucleation and growth occurs. Concentrations of catalyst particles significantly above 1×10^{14} #/m³, however, lead to poor control over catalyst particle size and polydispersity at the CNT nucleation front which, in turn, leads to poor control over CNT diameter. The location of the growth window is, shown to be directly associated with the availability of catalytically produced CO₂ diffusing from the reactor walls to the reactor core. These results help to explain the large variations in CNT diameter and chirality and the inefficient use of catalyst material in other floating catalyst CNT processes based on *in-situ* catalyst particle synthesis.

Keywords: Carbon Nanotubes, CNT, Computational Fluid Dynamics, CFD, Catalyst, Aerosol, Particle, Method of Moments, Evaporation, Coagulation, Population Balance, Chemical Kinetics.

1. INTRODUCTION

Carbon nanotubes (CNTs) are of interest due to their unique electrical, structural, chemical, thermal and optical properties, however, many applications of CNTs require large volumes of functionally similar material having a narrow range of properties such as diameter, length and chirality. For instance, Single-Walled CNTs (SWCNTs) can range from wide band gap semiconductors to metallic depending upon their chiral index.¹ It is known that, for aerosol (floating catalyst) Chemical Vapor Deposition (CVD) synthesis methods, the size of catalyst particles is critical in determining CNT diameter and thus, to some extent, the chirality and that residence times under growth conditions help to determine CNT length.² Consequently,

controlling catalyst particle sizes and residence times in growth environments are important requirements for ultimately controlling the properties of produced CNTs. Poor control of these parameters can lead to low efficiency in the use of catalyst material, production of significant amounts of carbon materials other than CNTs and wide distributions of CNTs properties.

Traditionally, floating catalyst methods for CNT production have relied on *in-situ* formed catalyst particles produced from chemical precursors in the region of CNT nucleation and growth.^{3,4} These methods produce CNTs having wide distributions of diameter, length and chirality and result in product containing a significant amount of unused catalyst material and amorphous carbon which requires further purification steps. Recently, we have developed a novel aerosol method for the synthesis of CNTs relying on the introduction of well controlled

* Author to whom correspondence should be addressed.

[†] Present address: Canatu Oy, Tekniikantie 21, Espoo, 02150, Finland

pre-made catalyst particles into an aerosol reactor via a hot wire generator (HWG).⁵ It was shown that the method is useful for the production of both single-walled⁵ and multiwalled⁶ CNTs with controllable dimensions of catalyst particles and CNTs.² In this work, we aim to understand the role of catalyst particle evolution in CNT synthesis by modeling the flow, heat transfer, gas phase species production and transport as well as particle transport and dynamics in our reactor.

Other work on the reactor level modeling of CNT production can be found in the literature, however, no previous models have yet been applied to predict polydisperse CNT catalyst particle dynamics and transport. The simplest reported modeling studies neglect the catalyst particle dynamics and model only the reactor flow and temperature conditions (e.g., Ref. [7]). Scott et al.⁸ have studied the HiPCO process⁴ by using the results of Eulerian calculations of the flow inside the reactor as temperature boundary conditions for trajectory calculations of iron cluster dynamics. Cluster calculations included detailed reaction mechanisms for a family of iron carbonyls and the growth of Fe_n and Fe_nCO clusters for n up to 999. Importantly, Scott et al.⁸ did not include cluster collision processes in their model. Endo et al.⁹ and Kawana et al.¹⁰ developed a CFD model that focuses on the chemistry of nanotube synthesis but did not consider the catalyst particle transport or dynamics in the reactor.

The computation of catalyst particle dynamics in CNT reactors can be carried out using a variety of numerical techniques, but such phenomena are usually modelled by solving the flow and gas phase partitioning in an Eulerian reference frame and tracking particles through the flow field in a Lagrangian reference frame. For highly diffusive particles, statistical accuracy requires a large number of trajectories and small time steps to account for Brownian motion. Significant reductions in computational effort can be achieved using an Eulerian formulation for multi-phase processes. In general, these can be classified as monodisperse methods, discrete population balance (DPB) (or sectional methods) and moment methods. Recently, Kuwana and Saito extended their CNT reactor model to include nucleation and growth of catalyst particles assuming monodispersity via a two moment method.¹¹ In this work, we use a three moment method in which the problem of mathematical closure is addressed by assuming the distribution is lognormal,¹² thus allowing the polydispersity of the Particle Size Distribution (PSD) also to be computed.

In this paper this validated model is used as a predictive and diagnostic tool to understanding factors that influence the control of CNT synthesis in floating catalyst methods. In particular, we investigate the behavior of pre-made catalyst particles up to the location of the experimentally observed CNT nucleation front. The influence of iron vapor concentrations at the reactor wall and fed particle size, number concentration and polydispersity are

computationally investigated and correlated with CO wall reaction kinetics and the transport of produced CO_2 .

2. MODELED EXPERIMENTAL SETUP

Our method for the production of SWCNTs has been described elsewhere.^{5,6} In the method, pre-made catalyst particles of controlled size, concentration and polydispersity are introduced into well defined synthesis conditions. Briefly, in this method, Fe particles were produced from Fe vaporized from a resistively heated catalyst wire in a H_2/N_2 (with a 7/93 mol ratio) flow ($400 \text{ cm}^3/\text{min}$). Here, particles were formed and grown by vapor nucleation, condensation and particle collision processes. Subsequently, the produced particles were introduced into either a ceramic or stainless steel tubular reactor, mixed with a carbon monoxide flow ($400 \text{ cm}^3/\text{min}$) and heated to induce CNT formation. Reactor wall peak temperatures ranged from 1163 K to 1480 K. In our first experiments, iron and carbon monoxide were used as the catalyst material and the carbon source, respectively. Experimental observations of CNT synthesis behavior in the reactor at a peak wall temperature of 1197 K concluded that there is a specific “growth window” for CNT nucleation and growth in which all CNT synthesis occurred, however, CNT production was unstable.¹³ Further analysis of the experimental data showed that these instabilities were primarily associated with the reactor wall conditions. It was found that, in order to provide reproducible CNT synthesis conditions, the reactor walls had to be saturated with iron. This was achieved either by deposition of iron particles on the reactor walls or by using reactor tubes made principally of iron, i.e., stainless steel. Depending on the level of iron saturation at the wall, it was observed that CNTs did or did not form. Reactors with iron saturated walls (either via the stainless steel reactor wall tube or by preconditioning with iron vapor and/or particles) were found to produce CNTs while reactors with “clean” walls (unconditioned ceramic) produced no CNTs. At these conditions, the growth window was determined to be between 1167 and 1179 K in the heating region of the reactor¹³ when the wall reaction temperature was 1480 K. This temperature coincides with the results reported in Ref. [5], where the growth of CNTs in a ceramic tube was observed above a maximum reactor temperature of 1163 K. Similar temperature windows for CNT growth were found with CNT production via thermal decomposition of ferrocene.¹⁴ From this data, we developed the hypothesis that the iron vapor pressure at the reactor wall were critical in stabilizing catalyst particles by reducing or eliminating catalyst particle evaporation before CNT nucleation.

In the current modeling work, boundary conditions are chosen to simulate conditions wherein reactor walls were saturated and unsaturated with iron at the highest temperature reactor experimentally investigated in Ref. [13] (with a

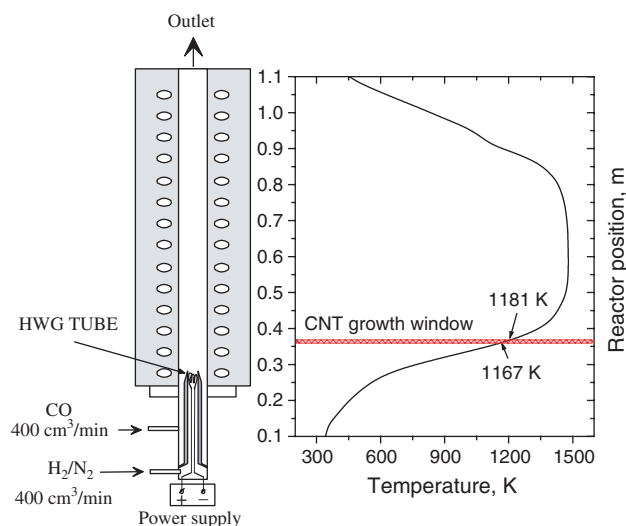


Fig. 1. Schematic of modeled experimental setup showing the wall temperature profile and the location of the CNT “growth window.”

maximum reactor temperature of 1480 K) where, it would be expected, particle dynamics would be most pronounced. A schematic of the experimental apparatus together with measured reactor wall temperatures specifying the location of the growth window is shown in Figure 1. Based on these conditions, a series of CFD calculations was performed to investigate catalyst particle dynamics and gas phase species composition.

3. MODEL EQUATIONS AND BOUNDARY CONDITIONS

Our previous work has modeled polydisperse aerosol transport in two and three-dimensions as well as the effects of chemical reaction and gas phase species mixing and strong heat and mass transfer coupling on the evolution of the aerosol size distribution.^{15–19} This method uses an Eulerian moment form of the general dynamic equation for aerosol behavior developed using a lognormal size distribution in conjunction with a Reduced Navier-Stokes (RNS) formulation²⁰ for bulk fluid modeling with Mach number based streamwise pressure flux splitting and axial viscous terms included as a deferred corrector.

Three sets of governing equations are considered: those related to the transport of mass, momentum and energy in bulk fluid flow, those related to the conservation of individual species in the fluid and those related to the transport and dynamics of suspended particles within the fluid flow. For all cases studied, the local Reynolds number based on the inlet diameter was below 500 and the Grashof number was greater than unity indicating laminar flow under the influence of buoyancy. Details of the formulation, coupling and implementation can be found in Refs. [17–19]. A brief summary, including additions to the model needed for the present calculations, are given below according to the variable definitions described in the Nomenclature Section.

The bulk fluid flow is described by the compressible Reduced Navier-Stokes²⁰ equations with a deferred-corrector (DC)²¹ to recover the Full Navier-Stokes solution. In non dimensional form, the governing equations with source terms due to fluid/aerosol particle coupling and with multiple species in the gas phase including the effects of buoyancy in each coordinate direction ($\rho g_{\xi, \eta, \zeta}$) can be written in vector form as

$$\begin{aligned} & \text{diag}\left(1, 1, 1, 1, \frac{1}{\rho_f}\right) \frac{\partial}{\partial t} \begin{bmatrix} \rho \\ \rho u_f \\ \rho v_f \\ \rho w_f \\ H_t - (\gamma - 1)M^2 P \end{bmatrix} \\ & + \frac{\partial}{\partial \xi} \begin{bmatrix} \rho U_f \\ \rho U_f u_f + \xi_x P - \tau_x^\xi \\ \rho U_f v_f + \xi_y P - \tau_y^\xi \\ \rho U_f w_f + \xi_z P - \tau_z^\xi \\ U_f H_t - \Phi_\xi + q_\xi \end{bmatrix} \\ & + \frac{\partial}{\partial \eta} \begin{bmatrix} \rho V_f \\ \rho V_f u_f + \eta_x P - \tau_x^\eta \\ \rho V_f v_f + \eta_y P - \tau_y^\eta \\ \rho V_f w_f + \eta_z P - \tau_z^\eta \\ V_f H_t - \Phi_\eta + q_\eta \end{bmatrix} \\ & + \frac{\partial}{\partial \zeta} \begin{bmatrix} \rho W_f \\ \rho W_f u_f + \zeta_x P - \tau_x^\zeta \\ \rho W_f v_f + \zeta_y P - \tau_y^\zeta \\ \rho W_f w_f + \zeta_z P - \tau_z^\zeta \\ W_f H_t - \Phi_\zeta + q_\zeta \end{bmatrix} = \begin{bmatrix} \Delta m \\ \rho g_\xi \\ \rho g_\eta \\ \rho g_\zeta \\ \Delta H_t \end{bmatrix} \quad (1) \end{aligned}$$

As, for the cases computed in the work, the mass fraction of particles is low, ΔH_t is assumed to be zero. Closure of the equations is achieved with the equation of state.

$$\gamma_\infty M_\infty^2 \frac{C_p}{R} P = \rho \left(H_t - \frac{1}{2} (\gamma_\infty - 1) M_\infty^2 (u^2 + v^2 + w^2) \right) \quad (2)$$

The total enthalpy of the mixture is defined as

$$H = \frac{u_f^2 + v_f^2 + w_f^2}{2} + \sum_{s=1}^{N_s} C_s h_s = \frac{u_f^2 + v_f^2 + w_f^2}{2} + h \quad (3)$$

according to the formulation given in.¹⁸

The present method uses an Eulerian moment form of the general dynamic equation (GDE) developed assuming a lognormal size distribution,^{12,22} which has been found to exist in a wide range of aerosol systems.²³ The model incorporates contributions for particle transport (due to

convection, diffusion and thermophoresis) and dynamics (due to coagulation, evaporation and condensation). Nucleation is not considered in this work since the high concentrations of catalyst particles introduced into the reactor provides sufficient surface area for condensation alone to maintain low supersaturation ratios throughout the reactor, thus eliminating the formation of additional particles.¹⁶ In non-dimensional form, the GDE yields a moment form representing three simultaneous partial differential equations, thus

$$\begin{aligned} \rho \frac{\partial (M_k/\rho)}{\partial t} + \rho \mathbf{U}_f \cdot \nabla (M_k/\rho) \\ - \nabla \cdot \left(\frac{1}{Sc_k Re_l} \nabla M_k \right) + \nabla \cdot \left(M_k \frac{K_T}{Re_L T_f} \nabla T_f \right) \\ = \gamma_k M_k^2 M_{k\infty} t_\infty + \sum_{s=1}^{N_s} (K_{Cond} \alpha_{ks} (S_s - F_s) M_k) t_\infty \quad (4) \end{aligned}$$

where $k = 0, 1, 2$. In this work, α_c and K_{Cond} are assumed to be unity. The polydisperse Schmidt numbers (Sc_k) are given in Ref. [19]. In general, the coagulation and condensation/evaporation terms take different forms for continuum, slip, and free molecular regimes. One set of equations is used for all regimes by using a harmonic average of the continuum and free molecular equations.¹²

A separate continuity equation is required for each gas phase species. Thus, for all species s , the saturation equation takes the form

$$\frac{\partial \rho C_s}{\partial t} + \nabla \cdot \left[C_s \left(\mathbf{U}_f - \frac{1}{Sc_s Re_l} \nabla (\ln C_s) \right) \right] = \Delta m_s \quad (5)$$

where C_s is the gas phase mass fraction for species s . The RHS represents the sources in mass due to evaporation, condensation and chemical reaction. Coupling source terms for mass transfer between the bulk flow, individual gas phase species and aerosol moments are determined from the relevant system parameters via

$$\Delta m = \sum_{s=1}^{N_s} (\Delta m_s) = \sum_{s=1}^{N_s} (-\alpha_{1s} (S_s - F_s) M_1) \quad (6)$$

where Δm appears in the bulk flow continuity and Δm_s appears in each species equation.

Flow, species and aerosol behavior are computed in separate modules using a finite difference discretization

scheme and simultaneously marched in space based on the principles of the RNS methodology.²⁰ Multiple sweeps are required to converge the axial diffusion and axial pressure terms. Details of the discretization of the governing equations, implementation of boundary conditions, numerical coupling, matrix inversion routines and the local and global solution procedure are described in.^{17, 18}

4. COMPUTATIONS OF GAS AND PARTICLE DYNAMICS IN MODEL CNT REACTOR

In order to assess the impact of catalyst particle source size and concentration as well as wall conditions on catalyst particle dynamics in the CNT growth window, a series of computations have been carried out. Case 1 investigates overall effect of reactor conditions (temperature, velocity and iron concentration) on the direction of the driving force for particle evaporation/condensation. Cases 2 and 3 additionally consider inlet and wall saturation conditions together with the effects of evaporation kinetics. Cases 4 through 6 investigate the influence of catalyst particle concentration. Case 7 addresses the effect of CO₂ production at the wall on the gas composition in the CNT growth window. Boundary conditions for each of the cases described below are listed in Tables I and II. Physical constants used in the calculations are listed in Table III. All cases were calculated in axisymmetric two dimensional space and included buoyancy with gravity pointing in the negative axial direction (i.e., flow from bottom to top). Ranges for source catalyst particle geometric number mean diameters (between 1.78 nm and 3.00 nm), concentrations (between 1×10^{14} #/m³ and 1×10^{18} #/m³) and geometric standard deviation of the particle size distribution (1.2) were estimated based on experimental observations of collected samples²⁴ and particle size distribution measurements based on electrical mobility downstream of the reactor.²⁵

4.1. Case1: Base Calculation of Gas Flow and Heat Transfer

An initial single phase CFD computation was used to investigate the overall conditions in the reactor and, in particular, the direction of the driving force for particle

Table I. Reactor conditions and gas phase boundary conditions for cases 1–6.^a

Boundary condition	Velocity (m/s)	CO mole fraction	N ₂ mole fraction	H ₂ mole fraction	Pressure (Pa)	Temperature (K)
HWG Inlet	0.104793	0.465	0.465	0.07	Calculated	298.15
Coflow Inlet	0.026947	0.5	0.5	0.0	Calculated	298.15
Reactor Wall	0.0	dC/dn = 0	dC/dn = 0	dC/dn = 0	Calculated	Set from experimental data
Reactor Outlet	dV/dn = 0	dC/dn = 0	dC/dn = 0	dC/dn = 0	1.01325×10^5	dHt/dn = 0

^adx/dn = 0 implies a zero gradient boundary conditions.

Table II. Catalyst particle boundary conditions for cases 2–6.

Boundary condition	Case	Number concentration M_0 (#/m ³)	Geometric mean diameter D_p (nm)	Standard deviation of PSD σ_g (N.D.)	Fe vapor saturation ratio S (N.D.) at reactor wall
Catalyst	1	0.0	0.0	N.A	1.0
Particle	2	1×10^{14}	3.0	1.2	1.0
Source	3	1×10^{14}	3.0	1.2	0.0
Outlet	4	1×10^{14}	1.78	1.26	0.0
	5	1×10^{16}	1.78	1.26	0.0
	6	1×10^{18}	1.78	1.26	0.0
	7	0.0	0.0	N.A	0.0
Coflow Outlet	1–7	0.0	N.A	N.A	Calculated
Reactor Outlet	1–7	$dM_0/dn = 0$	Calculated	Calculated	Calculated

Table III. Properties of species used in calculations.

Value	Fe	N ₂	H ₂	CO ₂	CO	Unit
MW	55.847	28.013	2.016	44.010	28.010	g/mole
γ	N.A	1.40	1.41	1.28	1.398	ND
Pr	N.A	0.71	0.71	0.71	0.71	ND
ρ_p	7040	N.A	N.A	N.A	N.A	Kg/m ³
$\Sigma = A$	A = 2.41743	N.A	N.A	N.A	N.A	J/mol K
+ B T	B = -3.1363×10^{-4}					
+ C T ²	C = 2.5893×10^{-9}					
+ D T ³	D = 2.7590×10^{-13}					
Cp = A	A = 27.06	A = 25.845	A = 33.6667	A = 42.388	A = 25.6942	
+ B/T ²	B = 0	B = 47861	B = -7307.16	B = -889108	B = 110861	
+ C/T	C = 0	C = 0.00	C = -752.260	C = 0.00	C = 0.00	
+ D T	D = 0	D = 0.0089004	D = -0.0109767	D = 0.0150998	D = 0.008292374	
+ E T ²	E = 0	E = -2.3480×10^{-6}	E = 1.2322×10^{-5}	E = -2.9078×10^{-6}	E = -1.4769×10^{-6}	
+ F T ³	F = 0	F = 2.1164×10^{-10}	F = -4.7198×10^{-9}	F = 0.00	F = 0.00	
+ G T ⁴	G = 0	G = 0.00	G = 8.1436×10^{-13}	G = 0.00	G = 0.00	
+ H T ⁵	H = 0	H = 0.00	H = -5.2840×10^{-17}	H = 0.00	H = 0.00	
	(11.04482 – 18160.05715/T – 1.85945 $\times 10^6$ /T ² + 3.51941 $\times 10^8$ /T ³)					
Ps	10	N.A	N.A	N.A	N.A	Pa
σ	4.30	3.798	2.827	3.941	3.690	m ⁻¹⁰
ε_k	3000	71.4	59.7	195.2	91.7	K

evaporation in the absence of the influence of catalyst particles. In general, since particle mass loadings were low for all the later cases investigated, these flow field and temperature calculations are also valid for cases 2–7. Iron vapor concentration and saturation ratios, however, change considerably under different catalyst particle source concentration and wall saturation conditions. Figure 2 shows the conditions in the reactor under conditions in Table I, Case 1 where the walls are saturated with iron and particle effects on the gas phase are neglected. Flow is from left to right with gravity pointing in the negative axial direction. Temperatures were found to be uniform and the entire flow was heated to within 5 K of the peak reactor temperature (Fig. 2(a)). The hot reactor section extended from approximately 0.45 m to 0.8 m. The flow in the reactor was found to be without recirculation up to and including the observed CNT growth window between 1167

and 1179 K in the heating section (Fig. 2(b)) corresponding to a centerline location at approximately $x = 0.39$ (0.14 meters from the HWG exit). Figure 2(c) shows the iron vapor concentration in the absence of iron catalyst particles and with iron saturated reactor walls. Iron vaporized from the walls was found to be relatively uniform across the reactor and reached a peak vapor mass fraction of approximately 1.1×10^{-7} near the hottest section and then decreasing as excess iron condensed on the reactor walls. By the reactor exit, the iron vapor concentration dropped below 1×10^{-9} . The effective saturation ratio for a given particle size including the Kelvin effect (taking into account the particle surface curvature) is defined as

$$S^* = \frac{P_{Fe}^*}{P_{eq}^*} \exp \left[\frac{-2\Sigma^* v_1^*}{r^* k_B T_f^*} \right] \quad (7)$$

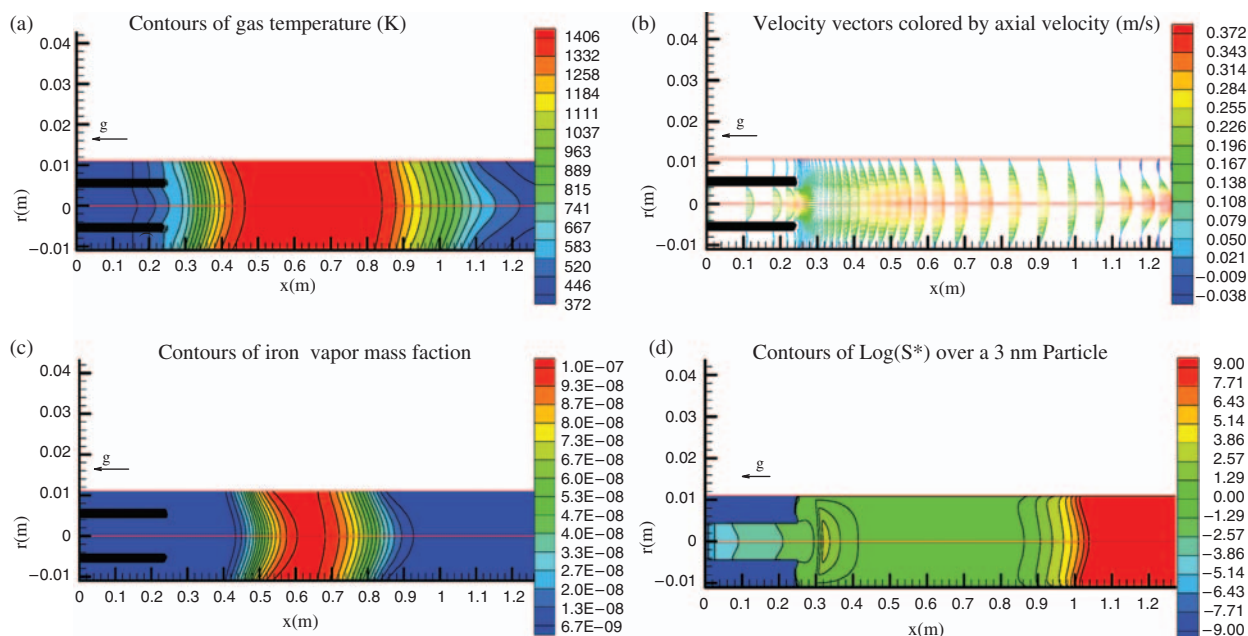


Fig. 2. Gas temperature (a), velocity vectors shaded by axial velocity (b), iron vapor mass fraction (c), and effective saturation ratio for 3 nm iron particles (d), in the modeled reactor with no introduced pre-made particles at a wall peak temperature of 1480 K with coflow and particle source flow rates of 400 cm³/min.

S^* less than unity implies that particles will tend to evaporate. Figure 2(d) shows an example of the calculated effective saturation ratio for 3 nm particles based on the expectation that evaporation would drive particles toward the observed diameter of 1.78 nm. Smaller particles have a higher effective saturation pressure and thus a stronger driving force for particle evaporation. Even for these relatively large catalyst particles, S^* is less than 1 from approximately $x = 0.41$ to $x = 0.85$ m. It is apparent that, even in the presence of iron saturated walls there is a driving force for particle evaporation and particles will tend to be reduced in size in the majority of the reactor. This calculation, however, does not take into account the kinetics of particle evaporation that would tend to reduce this driving force. Under the same flow rates and reactor temperature as in Case 1, additional cases were computed according to conditions in Table II in order to estimate these kinetic effects. Note that for clean ($S = 0$) reactor walls, there is no additional source of iron vapor and there always a driving force for catalyst particle evaporation. For brevity, results are not shown here.

4.2. Cases 2–3: Effect of Wall Saturation Conditions Catalyst Particle Evaporation

In Cases 2–3 the particle geometric number mean size, number concentration and standard deviation of the size distribution were kept constant while the wall concentration of iron vapor was varied in order to study the effects of wall saturation conditions on the resultant catalyst cluster dynamics. Calculations of the particle transport and dynamics were performed downstream from the

source outlet plane at $x = 0.25$ until the reactor outlet. We assume a continuous change of particle size when, in fact, the evaporation process is discrete (atom by atom). As a lower bound, however, particle evaporation was halted when geometric mean diameter reached that of two iron atoms. Again, a source particle mean diameter of 3 nm was chosen. A source particle number size distribution of 1×10^{14} #/m³ was estimated based on experimentally observed concentrations at the outflow based on aerosol measurements. Note that the particle source concentrations are absolute values and are not normalized. A source particle geometric standard deviation of the PSD of 1.2 was measured from High Resolution Transmission Electron Microscopy images.²

Calculations showed that, at these conditions, particle concentrations were sufficiently low for inter-particle collisions and particle-to-gas coupling to be unimportant. Figures 3(a–c) shows the evolution of particle number concentration, mass fraction and geometric number mean size at the iron saturated wall condition. In Figure 3(a) we can see that the particle number concentration initially drops due to the reduction of gas density in the heating zone. The concentration then rapidly decreases at approximately $x = 0.51$ as clusters evaporate down to di-atoms and then rapidly diffuse to the reactor walls. In Figure 3(b) we can see the simultaneous effects of particle diffusion and evaporation. As the particles move downstream, there is initially diffusion in the radial direction which spreads the particle stream. At approximately $x = 0.44$ m, particles begin to evaporate at an increasing rate due to the increased relative surface area and stronger Kelvin effect.

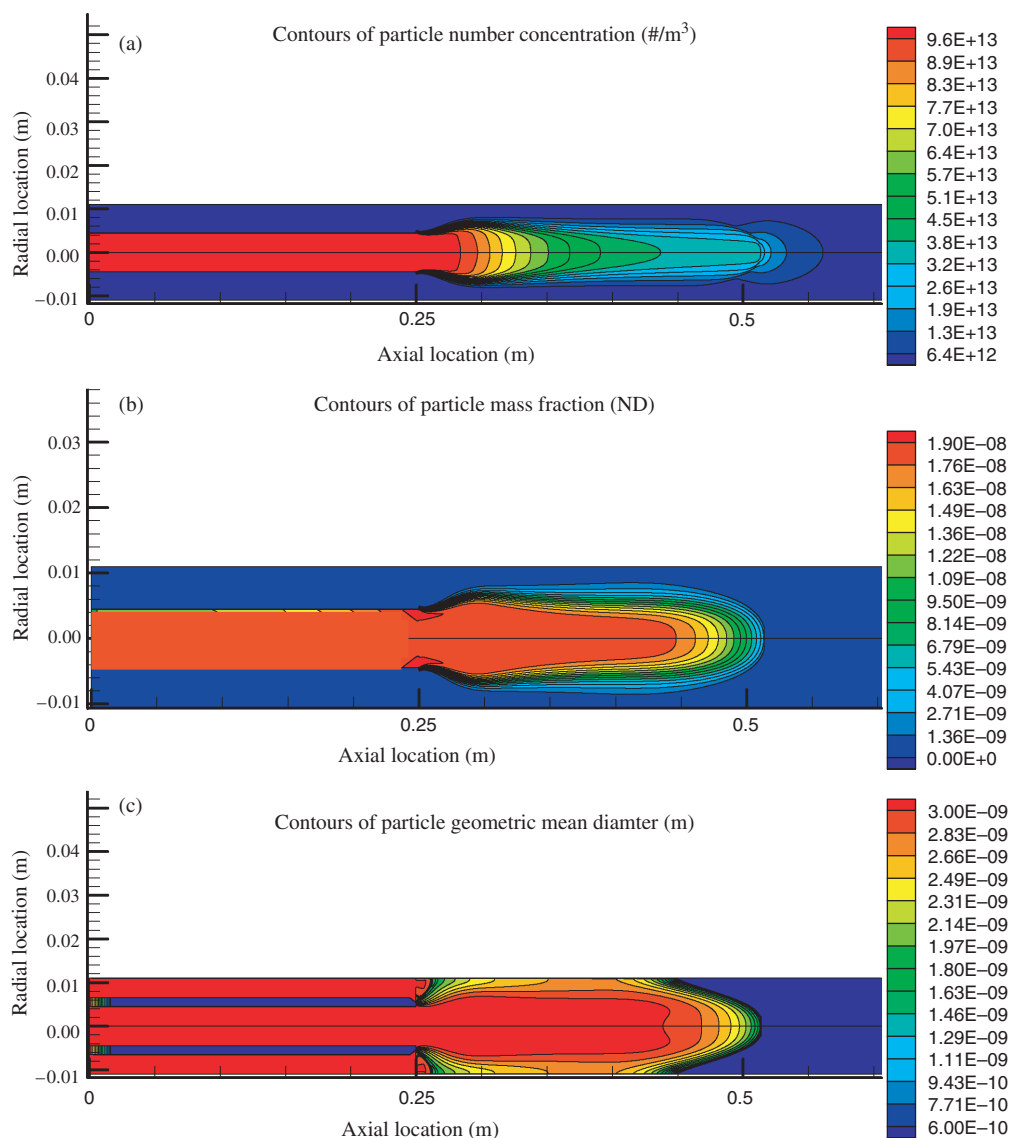


Fig. 3. Particle number concentration (a), mass fraction (b), and geometric number mean particle diameter (c), contours for 3 nm pre-made particles at a source concentration of 1×10^{14} #/m³ and a PSD geometric standard deviation of 1.2. Walls are saturated with iron.

Figure 3(c) shows the evolution of particle diameter in the reactor. Here the simultaneous effects of preferential diffusion and evaporation can be seen. Due to their higher diffusivity, smaller particles diffuse more rapidly in the radial direction than larger particles. Thus the average particle size is smaller near the reactor wall than at the reactor core. Rapid particle evaporation occurs between $x = 0.41$ and 0.51 m.

Overall, particles were found to be stable up to approximately 0.18 m from the source outlet ($x = 0.43$ m) and did not evaporate until approximately 0.26 m downstream ($x = 0.51$ m). All particles survived with no appreciable reduction in size up to the experimentally measured CNT growth window 0.14 m from the source outlet ($x = 0.39$ m). Lowering the iron vapor concentration at the reactor walls (simulating a clean ceramic reactor tube) produced virtually identical results (less than a 1 mm

difference in the location of particle evaporation) indicating wall saturation conditions do not play a significant role in particle evaporation dynamics and thus are not important in explaining either the initiation or the termination of CNT synthesis in the observed CNT growth window.

4.3. Cases 4–6: Effect of Inlet Catalyst Particle Concentration on Particle Dynamics

In order to determine the effect of catalyst particle concentration on CNT growth dynamics, Cases 4–7 were computed by keeping the wall saturation conditions as well as particle geometric mean diameter and standard distribution of the particle size distribution (1.78 nm and 1.26 respectively) constant and varying the particle source concentration from 1×10^{14} to 1×10^{18} #/m³. Figure 4 to Figure 7 show the dramatic effect of increasing the inlet

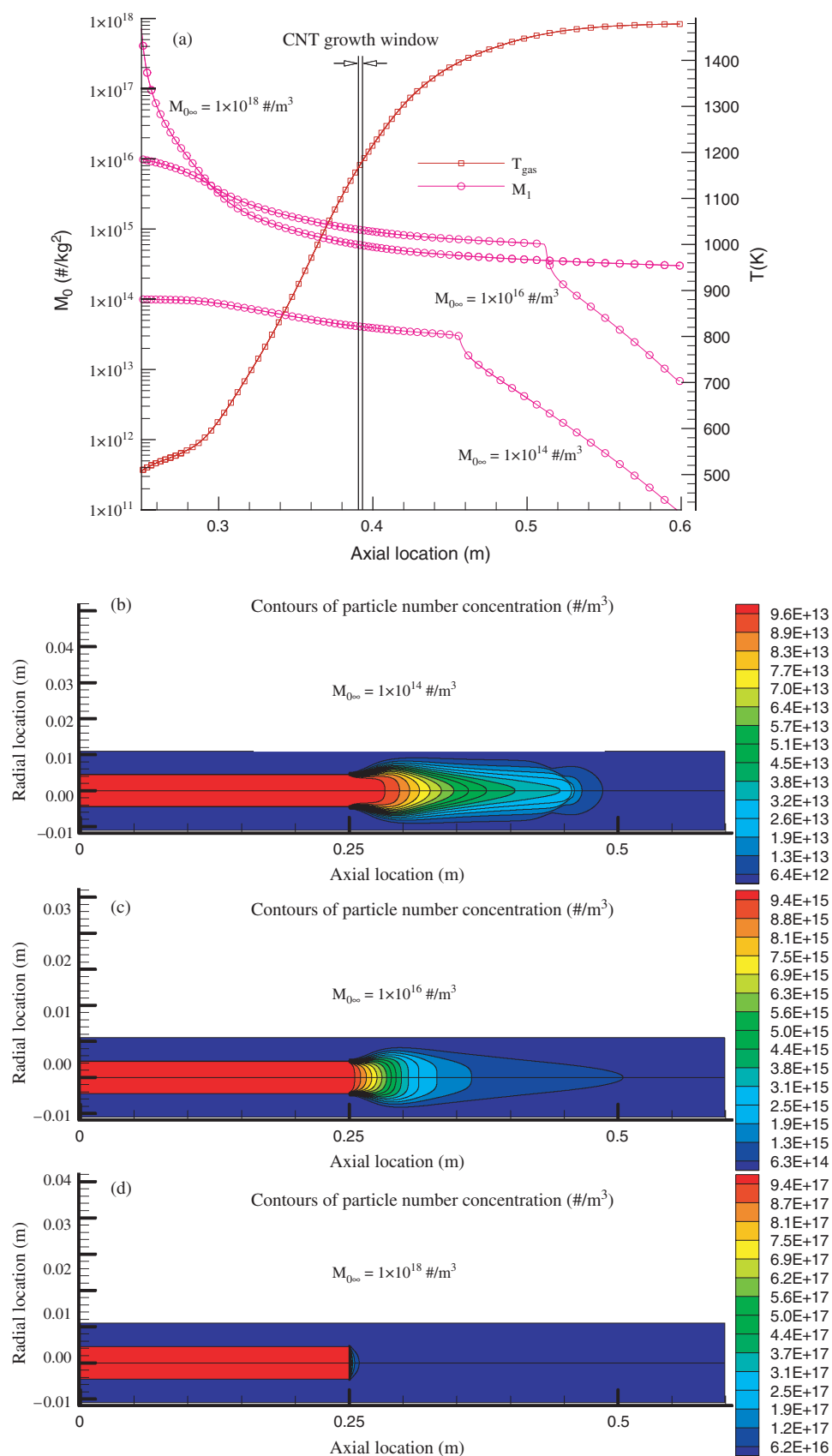


Fig. 4. Particle number concentration along the centerline (a), of the reactor at a wall peak temperature of 1480 K for source particle concentrations of 1×10^{14} , 1×10^{16} and $1 \times 10^{18} \text{ \#}/\text{m}^3$ and particle number concentration contours for each inlet concentration (b, c, and d).

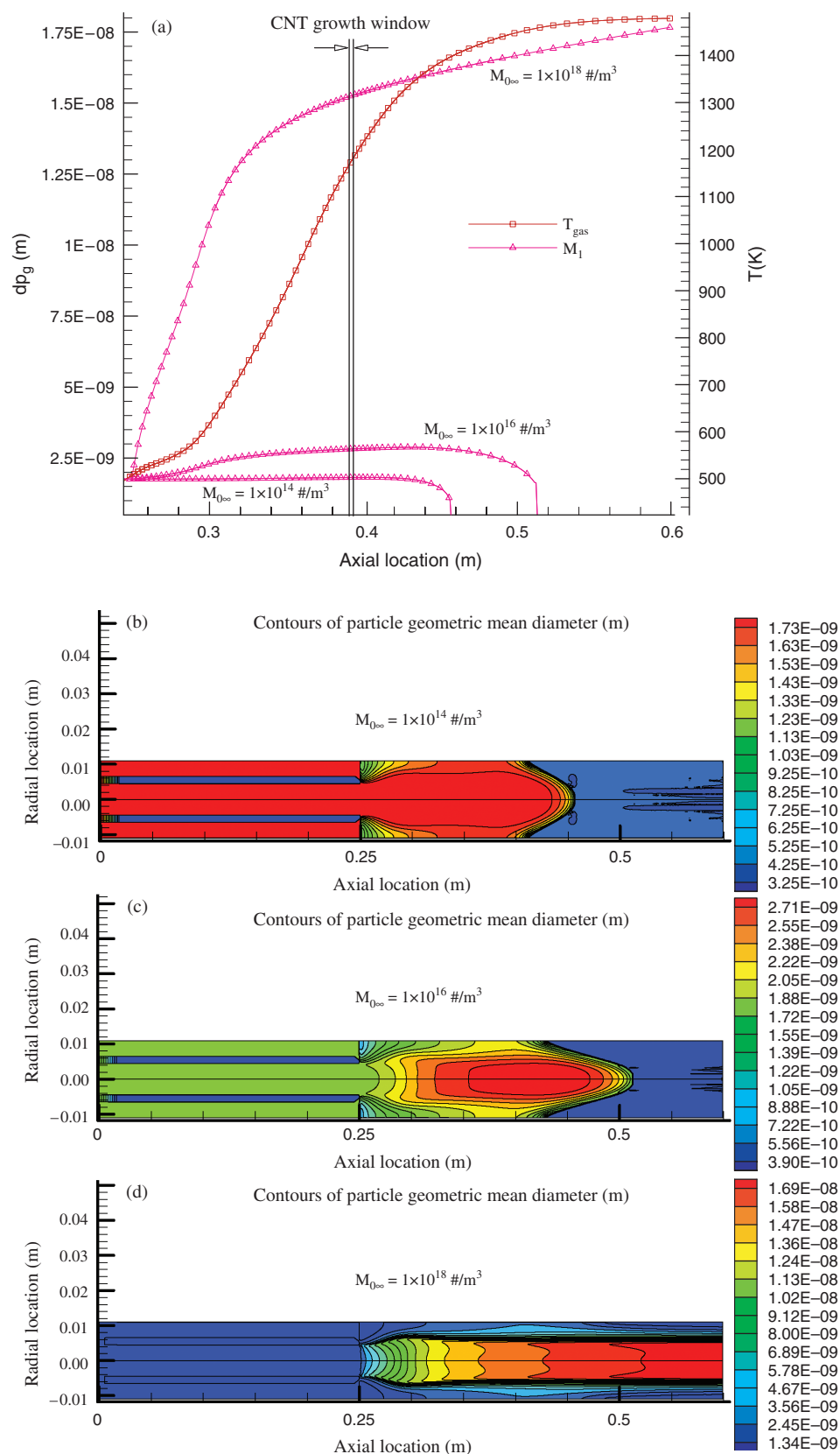


Fig. 5. Particle diameter along the centerline (a), of the modeled reactor at a wall peak temperature of 1480 K for source particle concentrations of 1×10^{14} , 1×10^{16} and $1 \times 10^{18} \text{ \#/m}^3$ and particle diameter contours for each inlet concentration (b, c, and d).

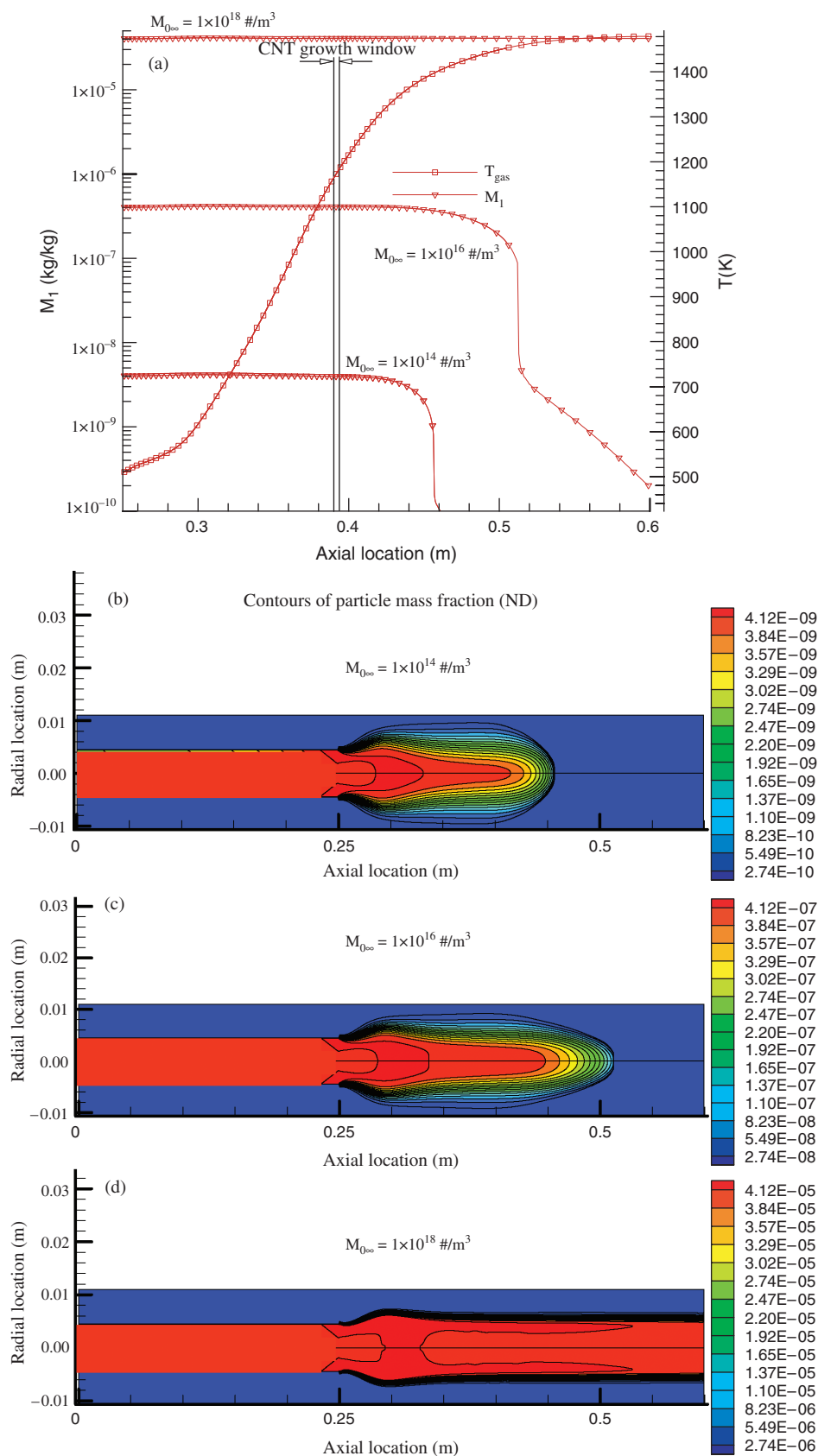


Fig. 6. Particle mass fraction along the centerline (a), of the modeled reactor at a wall peak temperature of 1480 K for source particle concentrations of 1×10^{14} , 1×10^{16} and $1 \times 10^{18} \text{ \#}/\text{m}^3$ and particle mass fraction contours for each inlet concentration (b, c, and d).

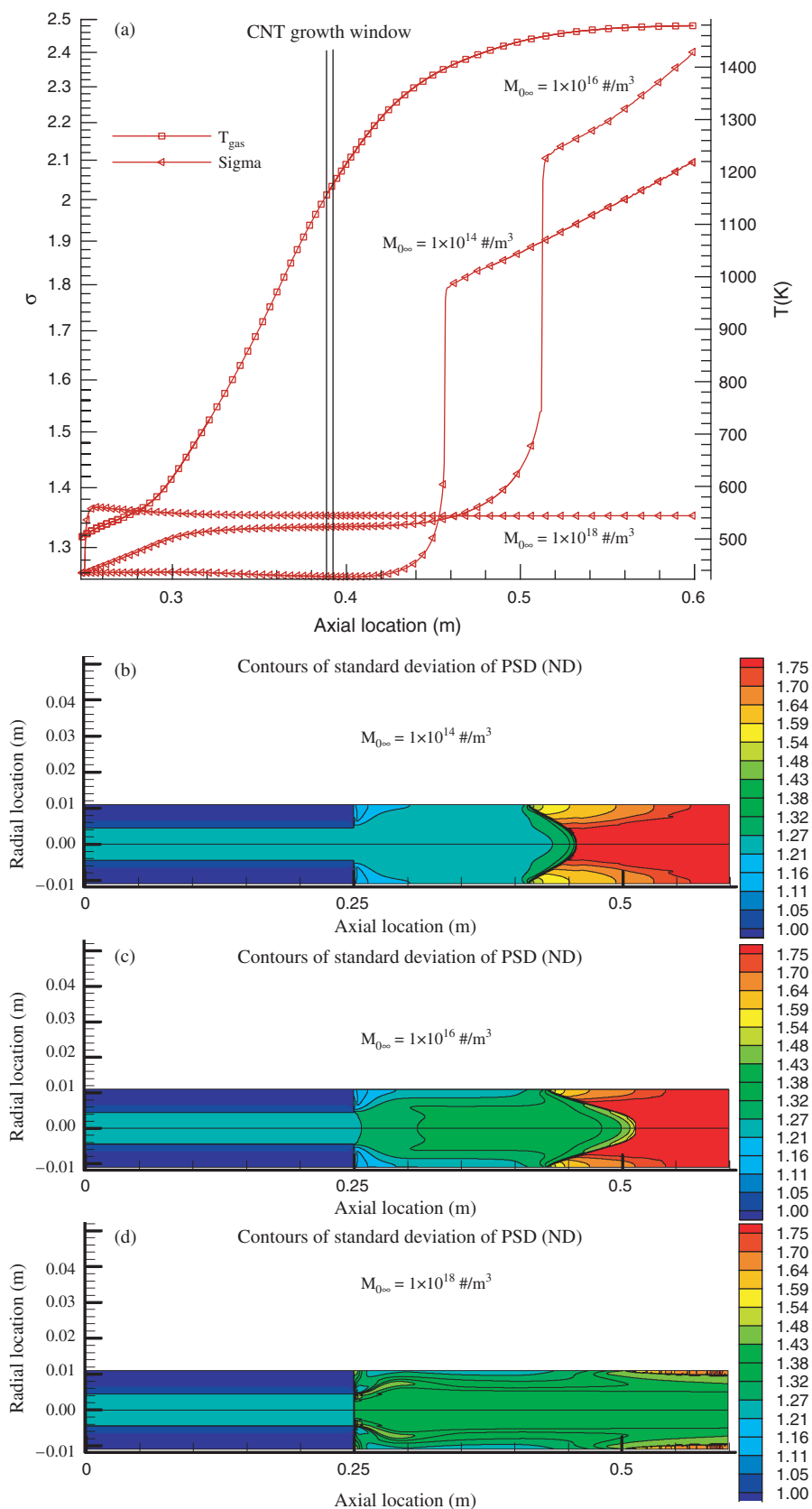


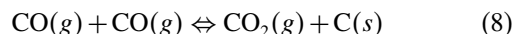
Fig. 7. Standard deviation of the PSD along the centerline (a), of the modeled reactor at a wall set temperature of 1200 C for source particle concentrations of 1×10^{14} , 1×10^{16} and $1 \times 10^{18} \text{ \#/m}^3$ and standard deviation of the PSD contours for each inlet concentration (b, c, and d).

particle number concentration on the catalyst particle size and size distribution in the reactor. In all cases, particles are stable up to and including the observed CNT growth window at $x = 0.39$ m, however, higher particle concentrations result in significant particle collisions and cause the particle number concentration to decrease (Fig. 4). Higher initial concentrations lead to more rapid reduction rates (Fig. 4(a)). At the highest source concentration (1×10^{18} #/m³), the catalyst particle number concentration decreases by more than 3 orders of magnitude by the time particles are in the CNT growth window and are actually lower in concentration than if they had been introduced at a number concentration two orders of magnitude lower (1×10^{16} #/m³). The evolution of particle size is shown in Figure 5. Interparticle collisions and coagulation causes particles to grow and, at higher concentrations, the particles grow more rapidly (Fig. 5(a)). At the highest calculated source concentration, the particles are found to grow by almost a factor of 10 (from 1.78 to 15.0 nm) by the time they reach the CNT growth window. Such particles are generally too large to synthesize SWCNTs. As can be seen in Figure 5(b), 1.78 nm particles do not readily collide and coagulate into larger particles at a source concentration of 1×10^{14} #/m³, but do diffuse more rapidly than the 3 nm particles of Cases 2 and 3 leading to a more even radial distribution in the reactor. They are found to evaporate approximately 0.05 m earlier than the 3 nm particles. Figure 5(c) shows that 1.78 nm particles introduced at a concentration of 1×10^{16} #/m³ grow to approximately 3 nm near the centerline before evaporation begins and to approximately 2 nm near the wall. These particles evaporate at approximately $x = 0.51$ m. At the highest source concentration, particles grow large enough not to evaporate and are able to exit the reactor intact (Fig. 5(d)). This is due to a reduced Kelvin effect, a reduced ratio of surface area to particle mass and an increase in the iron vapor mass fraction due to evaporation from particles. Additionally, these particles have very low diffusivity and remain close to the reactor centerline in a well defined column. The combined effects of particle collisions on diffusion and evaporation are seen more clearly in Figure 6 showing that higher source concentrations lead to larger, less diffusive and more slowly evaporating particles. Not only do high concentrations of source particles increase the mean particle size, leading to a large fraction of “dead” catalyst particles that are too large to synthesize CNTs, but it also leads to a significant widening of the particle size distribution as can be seen in Figure 7, resulting in less control over CNT diameter and, consequently, chirality. At the highest source concentration (1×10^{18} #/m³), the geometric standard deviation rises to the theoretically limiting value of 1.355 approximately 0.05 m from their point of introduction. At the intermediate source concentration (1×10^{16} #/m³), the geometric standard deviation approaches but does not reach this limiting value. This explains why the

highest calculated source concentration (1×10^{18} #/m³) leads to a lower number concentration in the growth window: wider PSDs have increased collision efficiencies.

4.4. Cases 7: Prediction of CO₂ Production Due to Catalytic Wall Reactions

As is apparent from the previous calculations, iron catalyst particles are not expected to evaporate before the growth window under even the most severe reactor conditions and the lowest particle loadings. Consequently, the effect of catalytic wall reactions was investigated as an explanation of the experimental observations of CNT synthesis. CO₂ in the gas phase has been shown to promote the synthesis of CNTs.²⁶ The importance of having iron on the reactor walls can be explained by its catalytic activity in CO disproportionation and hydrogenation reactions that lead to the release of gaseous products, such as carbon dioxide (CO₂) and water (H₂O). It was shown that those gaseous components formed upstream on the reactor walls play an important role downstream in the region of the CNT growth. This hypothesis is supported by the work of Hata et al.²⁷ and Nasibulin et al.,¹⁴ who have recently demonstrated the importance of water vapor and CO₂ in providing conditions for efficient growth of CNTs. Thus, an additional series of calculations was carried out in order to determine the correlation of catalytically produced CO₂ to the location of the growth window. CO/CO₂ conversion data¹³ (Fig. 8) showed a kinetically limited region up to approximately 1170 K according to the reaction



and a thermodynamically limited region above approximately 1,170 K. From this data, we have calculated an activation energy (Ea) of 63 kJ/mole in the kinetic region and this reaction was incorporated as CO and CO₂ boundary

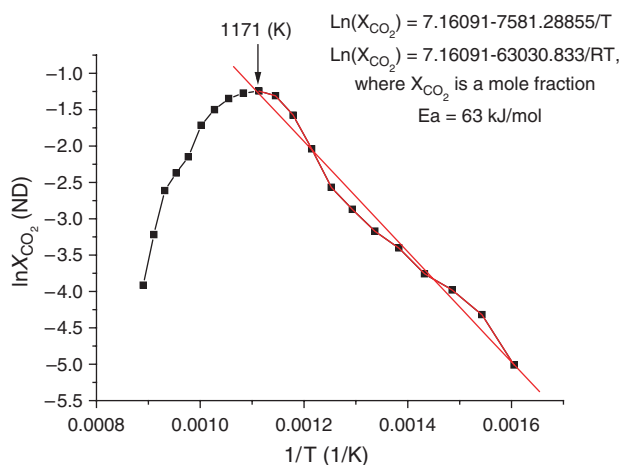


Fig. 8. Conversion of CO to CO₂ versus temperature showing kinetically limited and thermodynamically limited regions.

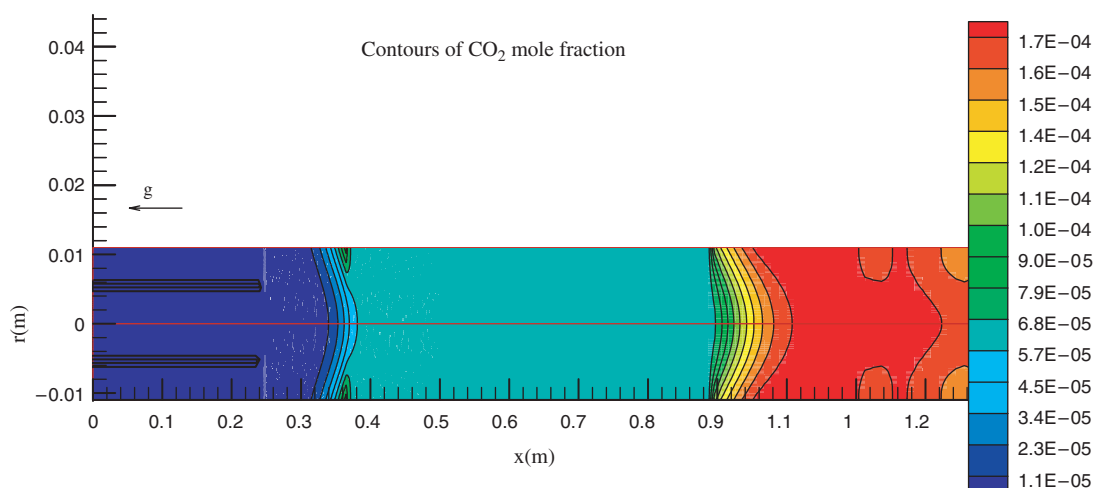


Fig. 9. CO_2 mass fraction contours in the modeled reactor showing catalytic production of CO_2 at the wall upstream of the observed CNT growth window.

conditions in the calculations such that, below the thermodynamic equilibrium state, CO conversion was limited kinetically according to reaction (8) with the rate of production of CO_2 is given by

$$\left(\frac{\partial C_{\text{CO}_2}}{\partial t} \right)_f = A_f \text{Exp} \left[-\frac{E_a}{RT_f^*} \right] C_{\text{CO}}^2 \quad (9)$$

Note that the reaction rate is then per unit area of the reactor wall. In the thermodynamics equilibrium region, the measured equilibrium concentration was used for the CO and CO_2 boundary conditions. Additionally we did not allow any catalytic decomposition reactions (kinetic or equilibrium) at walls where iron particles would be expected to be unstable. This lower limit was estimated to be 1200 K based on the earlier particle evaporation calculations. Experimental observations did not allow the accurate determination of the forward reaction rate A_f , however it was experimentally observed that, at the outlet of the reactor, the concentration of CO_2 was approximately 150 ppm as measured by Fourier Transform Infrared Spectroscopy (FTIR) when iron was present on the reactor walls. CFD calculations showed that assuming $A_f = 2.0 \times 10^{-3} \text{ mole}^{-1} \text{m}^{-2} \text{s}^{-1}$ gave similar outlet concentrations (Fig. 9). We did not consider the yield of H_2O since FTIR measured values were an order of magnitude lower than for CO_2 .²⁸ Figure 9 shows the mole fraction of CO_2 in the reactor clearly indicating that the location of the growth window approximately 0.18 m from the catalyst source outlet ($x = 0.43$) corresponds to a significant product concentration (approximately 80 ppm) and indicates a strong correlation between CNT formation and growth and the local availability of CO_2 .

As for the role of CO_2 in the reactor, several theories have been introduced. Adier et al.²⁸ reported CO_2 to be important to prevent the conversion of iron (Fe) to cementite (Fe_3C) which is likely to poison CNT catalyst particles. Nasibulin et al.²⁸ additionally reported the essential role of

CO_2 for the production of CNTs and, specifically, proposed it as an oxidizing agent that etches the surface of catalyst particles and CNTs and thus removes amorphous carbon which can block the introduction of additional carbon or poison the surface of catalysts and CNTs.

5. DISCUSSION

Calculations of the flow, heat transfer and gas and particle phase behavior of iron in the CNT reactor have revealed the insensitivity of the resulting catalyst particle size to wall Fe saturation conditions and the strong sensitivity of the resulting catalyst particle size and polydispersity to their initial size and concentration. In all cases and under the most extreme temperature conditions, even the lowest particle source concentrations ($1 \times 10^{14} \text{ \#/m}^3$) and smallest sizes (1.78 nm), catalyst clusters were found to be stable up to the observed CNT growth window. However, high concentrations resulted in significant particle growth by collision, effectively deactivating a large fraction of particles and widening their distribution. The resulting wider particle size distribution and increased mean diameter actually leads to an overall reduction in catalyst particle concentration in the growth window at the highest source concentrations calculated ($1 \times 10^{18} \text{ \#/m}^3$) as compared to the intermediate concentration ($1 \times 10^{16} \text{ \#/m}^3$). Consequently, large catalyst particle concentrations can, paradoxically, lead to lower yields of CNTs of lower homogeneity. Inflow concentrations should thus be kept below $1 \times 10^{16} \text{ \#/m}^3$ to maintain favorable properties for controlled CNT production. The composition of the reactor wall was found to be important, not due to the supply of iron vapor, as was originally believed, but, instead, due to its ability to supply CO_2 (through catalytic wall decomposition reactions) which is understood to enhance CNT nucleation and growth. Consequently, the likely role of the conditioning of the reactor wall was found to be

chemical (as a source of CNT precursor and/or promoter such as CO_2) rather than physical (as a source of sufficient Fe vapor to prevent evaporation). As the catalyst diameter in the active growth window is the critical factor in determining the diameter of synthesized CNTs, it is, therefore, vital to simultaneously control the concentration and diameter of catalyst particles and the concentration of CO_2 in important regions of the reactor in addition to the CO concentration and gas temperature.

It is useful to interpret these results in terms of the available literature for floating catalyst CNT production. For instance, in the HiPCO process,⁴ catalyst particles are generated *in situ* via the thermal decomposition of $\text{Fe}(\text{CO})_5$ vapor under high pressure conditions in a quartz reactor. It is known that a large fraction of catalyst particles remain inactive, that the distributions of catalyst particle size and produced CNT chirality are wide and that there is a significant amount of amorphous carbon remaining on the produced CNTs. This can be explained in terms of the catalyst particle production and collision dynamics and the availability of reagents such as CO_2 . In terms of the particle dynamics, in the HiPCO process, iron catalyst particles are produced continually in a wide reaction zone where the precursor gas decomposes to release supersaturated Fe vapor. This results in a large reaction zone where competition between nucleation and collision and high particle number concentrations tend to broaden their size distribution. Moreover, our results indicate that, since the HiPCO reactor has significant exposed surface area at moderate temperatures, one can expect the release of CO_2 from the reactor walls in the same manner as proposed in our reactor. In fact, as was reported in (Ref. [29]), a high concentration of CO_2 (on the order of 10,000 ppm) is known to exist at the HiPCO reactor outlet under CNT synthesis conditions. Though they have not reported CO_2 concentrations in the absence of $\text{Fe}(\text{CO})_5$ precursor, the presence of reactor walls and turbulent mixing (which leads to the deposition of iron on the walls) provides additional sources of CO_2 than from conversion on floating catalyst particles alone. Additionally, at high pressures the equilibrium of CO disproportionation reaction (1) is shifted towards the formation of CO_2 and C.³⁰ Thus, the high CO pressure effect is not only in the enhancement of the reaction rate due to an increase of the amount of reagent, but also in widening of the CNT formation temperature range and enlarging the growth window so that CNT growth occurs even up to 1500 K at 30 bars.³⁰ Thus, the high concentration of inactive catalyst particles having a wide size distribution in the HiPCO process can be explained as a result of the insufficient control of particle size due to their high concentration and continuous nucleation. Additionally, CO_2 concentration (which can inhibit coagulation and growth of active catalyst particles by initiating CNT growth) is unknown in the widened growth window.

Zhao et al.³¹ noted the importance of reactor conditions on the efficiency of catalyst use for CNT production from

sulfur contaminated ferrocene vapor. They reported that, for their experimental setup, reducing the diameter of the growth tube resulted in more efficient use of catalysts. This can be explained in terms of our current results in that smaller reactor tubes led to higher flow rates, and shorter residence times in the reaction zone. Shorter residence times further reduced the time for precursor decomposition and particle–particle interaction, thus maintaining a smaller and possibly narrower particle size distribution upon CNT nucleation, thus increasing yield efficiency.

Zheng et al.³² produced single-walled CNTs by a CVD method wherein they introduced CO gas pretreated in a 773 K furnace. They noted that the pretreatment furnace “was crucial to obtain clean single-walled CNT sample.” It was explained that the pretreatment was needed to remove $\text{Fe}(\text{CO})_5$ impurities in commercial CO. In the framework of our computations, however, we feel their result indicate that the pretreatment stage was necessary both to decompose $\text{Fe}(\text{CO})_5$ on the pretreatment reactor walls and to release CO_2 due to the CO disproportionation reaction on the deposited iron. Thus, their pretreatment reactor³² and our heated walls upstream of the growth window serve to provide CNT growth promoters (in this case CO_2) known to aid the synthesis of CNTs.

6. CONCLUSIONS

A CFD based polydisperse aerosol population balance model suitable for predicting the behavior of iron catalyst particles and surface reactions is used to understand the effects of catalyst particle size and concentration, surface CO disproportionation chemistry, heat transfer and wall saturation levels on catalyst particle size and synthesis conditions in floating catalyst synthesis methods. In this work, the dynamics of preformed catalyst particles introduced near the centerline of a heated tubular reactor into conditions leading to CNT nucleation and growth was simulated. It is found that introduced catalyst particles with diameters suitable for catalyzing SWCNTs do not evaporate until CNT nucleation under all studied reactor conditions. In particular, it is found that the level of wall iron vapor concentration does not significantly affect catalyst particle evaporation. However, catalyst particle concentrations significantly above $1 \times 10^{14} \text{ \#}/\text{m}^3$ lead to poor control over particle size and polydispersity at the CNT nucleation front which, in turn, is expected to lead to poor control over produced CNTs. The location of the experimentally observed growth window is shown to be associated with the availability of CO_2 produced by catalytic wall reactions and not with the stability of catalyst particles. Together, these results demonstrate the necessity of simultaneously controlling CO, CO_2 and catalyst particle size and concentration as well as gas temperatures and residence times in critical regions of the reactor in order to synthesize well controlled CNTs.

NOMENCLATURE

A_3	First coefficient of Schmidt number $\left(= \frac{\rho_f^* k_B T_f^*}{6\pi\mu_f^* r_{g\infty}^*} C \right)$	(ND)
A_4	Second coefficient of Schmidt number $\left(= \frac{\rho_f^* k_B T_f^*}{12\pi\mu_f^* r_{g\infty}^{*2}} 3.314\lambda^* \right)$	(ND)
b_0	$0.633 + 0.092\sigma^2 - 0.022\sigma^3$	(ND)
b_1	$0.39 + 0.5\sigma - 0.214\sigma^2 + 0.029\sigma^3$	(ND)
B_1	$(36\pi)^{1/3} v_1^* n^* \sqrt{k_B T_f^* / (2\pi m_1^*)}$	(m/s)
B_2	$\sqrt{6k_B T_f^* r_g^* / \rho_p^*}$	(m ³ /s)
B_3	$\frac{1}{3} \left((48\pi^2)^{1/3} \lambda^* v_1^* n_s \sqrt{8k_B T_f^* / \pi m_1^*} \right)$	(m ² /s)
B_4	$2k_B T_f^* / (3\mu_f^*)$	(m ³ /s)
C_c	Cunningham Correction Factor $C(v_p) = 1 + 1.257\lambda^* v_g^{*-1/3} \left(\frac{3}{4\pi} \right)^{1/3}$	(ND)
C	Mass fraction	(ND)
C_p	Mixture specific heat at constant pressure $\left(\sum_{s=1}^{N_s} C_s C p_s + C_a C p_a \right)$	(J/kg-K)
d	Diameter	(m)
D	Diffusion Coefficient $(k_B T_f^* \tau^* / m^*)$	(m ² /s)
E_a	Activation Energy	(J/mole)
F	Kelvin Effect Term $\left(\exp \left[\frac{2\sigma^* v_1^*}{r_g^* k_B T_f^*} \right] - 1 \right)$	(ND)
g	Jacobian of the coordinate transformation, acceleration of gravity	(ND, m/s ²)
G	Condensation rate	(m ³ /m ³ /s)
H_t	Total enthalpy	(m ² /s ²)
k	Reaction rate coefficient	(mole/m ² /s)
k_B	Boltzman's constant	(kg m ² /s ² /K)
K	Adjustable constant	(ND)
Kn	Knudsen Number (r_g^* / λ^*)	(ND)
K_T	Thermophoretic constant (= 0.55)	(ND)
L	Length	(m)
m	Mass	(kg)
M	Mach number of mixture $\sqrt{\frac{u_f^{*2} + v_f^{*2} + w_f^{*2}}{\gamma R T_f^*}}$	(ND)
M_k	k th volume moment of the distribution $M_k^* = \int_0^\infty v_p^{*k} n_p^*(v_p^*, t^*) dv_p^* = M_0^* v_g^{*k} \exp \left(\frac{9}{2} k^2 \ln^2 \sigma \right)$	(m ^{3k} /m ³)
MW	Mixture molecular weight $\left(\sum_{s=1}^{N_s} \rho_s C_s + \rho_a C_a \right) / \sum_{s=1}^{N_s} \frac{\rho_s C_s}{MW_s}$	(kg/mol)
$n(v)$	Particle number concentration	(#/m ³)
N_s	Number of gas phase species	(ND)
P	Pressure	(kg/m/s ²)
Pr	Prandtl Number $(C_p \mu_f / \kappa)$	(ND)
q	Heat flux	(kg/s ³)
R	Universal gas constant	(kg m ² /s ² /Kmol)
Re_l	Laminar Reynolds number $(\rho_\infty U_\infty L_\infty / \mu_{l\infty})$	(ND)
Re_L	Local Reynolds number $(\rho_f^* U_\infty L_\infty / \mu_f^*)$	(ND)
s	Surface area	(m ²)
S	Saturation ratio	(ND)

Sc	Schmidt number $\left(Sc = \frac{\mu_f^*}{\rho_f^* D_p^*} = \frac{\mu_f^{*2} 18 m_p^{*2}}{\rho_p^{*2} k_B T_f^* d_p^{*2} C} \right)$	(ND)
	$Sc_0 = 1/(A_3 v_g^{-1/3} \exp(0.5 \ln^2 \sigma) + A_4 v_g^{-2/3} \exp(2 \ln^2 \sigma))$	
	$Sc_1 = 1/(A_3 v_g^{-1/3} \exp(-2.5 \ln^2 \sigma) + A_4 v_g^{-2/3} \exp(-4 \ln^2 \sigma))$	
	$Sc_2 = 1/(A_3 v_g^{-1/3} \exp(-5.5 \ln^2 \sigma) + A_4 v_g^{-2/3} \exp(-10 \ln^2 \sigma))$	
T	Temperature	(K)
u, v, w	Cartesian components of velocity	(m/s)
U, V, W	Contravariant components of velocity	(ND)
U	Velocity vector	(ND)
v	volume $\left(v_g = \frac{M_1^2}{M_0^{1.5} M_2^{0.5}} \right)$	(m ³)
x, y, z	Cartesian coordinates in physical space	(m)
α_k	k th condensation coefficient	(ND)
	$\alpha_{0s} = 0, \quad \alpha_{1s} = \frac{\alpha_{1s}^c \alpha_{1s}^{fm}}{\alpha_{1s}^c + \alpha_{1s}^{fm}} \left(\frac{L_\infty}{U_\infty} \right), \quad \alpha_{2s} = \frac{\alpha_{2s}^c \alpha_{2s}^{fm}}{\alpha_{2s}^c + \alpha_{2s}^{fm}} \left(\frac{L_\infty}{U_\infty} \right)$	
	$\alpha_{1s}^c = B_{3s} v_g^{-2/3} \exp(-4 \ln^2 \sigma) \quad \alpha_{1s}^{fm} = B_{1s} v_g^{-1/3} \exp\left(-\frac{5}{2} \ln^2 \sigma\right)$	
	$\alpha_{2s}^c = B_{3s} v_g^{-2/3} \exp(-10 \ln^2 \sigma) \quad \alpha_{2s}^{fm} = B_{1s} v_g^{-1/3} \exp\left(-\frac{11}{2} \ln^2 \sigma\right)$	
β	Collision frequency function	(#/m ³ /s)
γ	Mixture ratio of specific heats $(1 - R/MW Cp)$	(ND)
γ_k	k th coagulation coefficient	(ND)
	$\gamma_0 = \frac{\gamma_0^c \gamma_0^{fm}}{\gamma_0^c + \gamma_0^{fm}} \left(\frac{M_{0\infty} L_\infty}{U_\infty} \right), \quad \gamma_1 = 0, \quad \gamma_2 = \frac{\gamma_2^c \gamma_2^{fm}}{\gamma_2^c + \gamma_2^{fm}} \left(\frac{M_{2\infty} L_\infty}{U_\infty} \right)$	
	$\gamma_0^c = -B_4 \left[1 + \exp(\ln^2 \sigma) + B_5 Kn \exp\left(\frac{1}{2} \ln^2 \sigma\right) (1 + \exp(2 \ln^2 \sigma)) \right]$	
	$\gamma_0^{fm} = -B_2 b_o v_g^{1/6} \left[\exp\left(\frac{25}{8} \ln^2 \sigma\right) + 2 \exp\left(\frac{5}{8} \ln^2 \sigma\right) + \exp\left(\frac{1}{8} \ln^2 \sigma\right) \right]$	
	$\gamma_2^c = \frac{2B_4}{v_g^2} \exp(-27 \ln^2 \sigma) \left[(1 + \exp(\ln^2 s)) + B_5 Kn \exp\left(-\frac{1}{2} \ln^2 \sigma\right) (1 + \exp(-2 \ln^2 \sigma)) \right]$	
	$\gamma_2^{fm} = \frac{2B_2 b_2}{v_g^{11/6}} \exp(-36 \ln^2 \sigma) \left[\exp\left(\frac{85}{8} \ln^2 \sigma\right) + 2 \exp\left(\frac{89}{8} \ln^2 \sigma\right) + \exp\left(\frac{109}{8} \ln^2 \sigma\right) \right]$	
Δ	Change due to aerosol formation and growth	(ND)
ε_k	Lennard-Jones Temperature	(K)
κ	Thermal conductivity	(kg/s ³ /K)
λ	Mean free path of gas mixture $\left(\lambda^* = \frac{\mu_f^*}{\rho_f^*} \sqrt{\frac{\pi m_s^*}{2 k_B T_f^*}} \right)$	(m)
ϕ	Knudsen correction $\left(\frac{2\lambda + d_p}{d_p + 5.33(\lambda^2/d_p) + 3.42\lambda} \right)$	(ND)
μ	Viscosity	(kg/m/s)
ρ	Mixture density $\sum_{s=1}^{N_s} \rho_s + \rho_a$	(kg/m ³)
σ	Standard deviation of aerosol size distribution	(ND, Å)
	$\left(\ln^2 \sigma = \frac{1}{9} \ln\left(\frac{M_0 M_2}{M_1^2}\right) + \ln^2 \sigma_\infty \right)$, Lennard-Jones Diameter	
Σ	Surface tension	(ND, N/m)
τ	Viscous stress tensor, characteristic time $\left(\tau = \frac{\rho_p^* d_p^{*2} C_c}{18 \mu_f^*} \right)$	(kg/m/s ² , s)
ξ, η, ζ	Transformed coordinates in computational space	(ND)

Subscripts

a	aerosol phase
j	ξ, η, ζ
Con	due to condensation
C	convective
D	diffusional
Eq	equilibrium
f	bulk fluid
g	geometric mean
k	k th aerosol moment
l	laminar
L	local
p	particle
s	gas phase species s
t	total
T	thermophoretic
v	viscous
w	wall value
Σ	surface tension
ξ, η, ζ	differentiated with respect to ξ, η, ζ
∞	initial, free stream or characteristic value

Superscripts

$*$	dimensional quantity
i	x, y, z
c	continuum
fm	free molecular
k	to the power k

Non-Dimensionalization

$$u = \frac{u^*}{U_\infty}, \quad x = \frac{x^*}{L_\infty}, \quad T = \frac{T^*}{T_\infty}, \quad \rho = \frac{\rho^*}{\rho_\infty}$$

$$P = \frac{P^*}{\rho_\infty U_\infty^2}, \quad t = \frac{t^*}{L_\infty / U_\infty}, \quad t_\infty = \frac{L_\infty}{U_\infty}$$

$$M_k = \frac{M_k^*}{M_{k\infty}^*}, \quad r_p = \frac{r_p^*}{r_{p\infty}^*}, \quad v_p = \frac{v_p^*}{\frac{4}{3}\pi r_{p\infty}^*}, \quad \rho_p = \frac{\rho_p^*}{\rho_{p\infty}^*}$$

Acknowledgment: Financial support from the Academy of Finland and the EU via the FP5 RTN “Nanocluster”-project are gratefully acknowledged. We would like to thank Dr. A. Krestinin for his valuable discussions regarding the possible role of CO₂.

References and Notes

1. M. S. Dresselhaus, G. Dresselhaus, and P. C. Eklund, *Science of fullerenes and carbon nanotubes*, Academic Press, San Diego (1996).
2. A. G. Nasibulin, P. V. Pikhitsa, H. Jiang, and E. I. Kauppinen, *Carbon* 43, 2251 (2005).
3. Y.-L. Li, I. A. Kinloch, and A. H. Windle, *Science* 304, 276 (2004).
4. P. Nikolaev, M. J. Bronikowski, R. K. Bradley, F. Rohmund, D. T. Colbert, K. A. Smith, and R. E. Smalley, *Chem. Phys. Lett.* 313, 91 (1999).
5. A. G. Nasibulin, A. Moisala, D. P. Brown, H. Jiang, and E. I. Kauppinen, *Chem. Phys. Lett.* 402, 227 (2005).
6. A. G. Nasibulin, A. Moisala, H. Jiang, and E. I. Kauppinen, *J. Nanopar. Res.* 8 465 (2006).
7. A. Povitsky and M. D. Salas, *AIAA Journal* 41, 2130 (2003).
8. C. D. Scott, A. Povitsky, C. Dateo, T. Gökçen, P. A. Willis, and R. E. Smalley, *J. Nanosci. Nanotechnol.* 3, 63 (2003).
9. H. Endo, K. Kuwana, K. Saito, D. Qian, R. Andrews, and E. A. Grulke, *Chem. Phys. Lett.* 387, 307 (2004).
10. K. Kuwana, H. Endo, K. Saito, D. Qian, R. Andrews, and E. A. Grulke, *Carbon* 43, 253 (2005).
11. K. Kuwana and K. Saito, *Carbon* 43, 2088 (2005).
12. Y. Xiong and S. E. Pratsinis, *J. Aerosol Sci.* 22, 637 (1993).
13. A. G. Nasibulin, P. Queipo, S. D. Shandakov, D. P. Brown, H. Jiang, P. V. Pikhitsa, O. V. Tolochko, and E. I. Kauppinen, *J. Nanosci. Nanotechnol.* 6, 1233 (2006).
14. A. Moisala, A. G. Nasibulin, D. P. Brown, H. Jiang, L. Khriachtchev, and E. I. Kauppinen, *Chem. Engg. Sci.* 61, 4393 (2006).
15. D. P. Brown, P. Biswas, and S. G. Rubin, *ASME FACT-Combustion Modeling, Scaling and Air Toxins* 18 (1994).
16. D. P. Brown, S. G. Rubin, and P. Biswas, *Sixth International Symposium on Computational Fluid Dynamics* (1995) Vol. 1, p. 129.
17. D. P. Brown, Ph.D. Dissertation, University of Cincinnati (1996).
18. D. P. Brown, NIST SBIR 97-1-58 Final Report (1998).
19. D. P. Brown, E. I. Kauppinen, J. K. Jokiniemi, S. G. Rubin, and P. Biswas, *Computers and Fluids* 35, 762 (2006).
20. S. G. Rubin and J. C. Tannehill, *Annual Review of Fluid Mechanics* 24, 117 (1992).
21. K. Srinivasan and S. G. Rubin, *J. Comput. Phys.* 136, 467 (1997).
22. H. Bai and P. Biswas, *J. Aerosol Sci.* 21, 629 (1990).
23. J. Heintzenberg, *Aerosol Sci. Technol.* 21, 46 (1994).
24. A. G. Nasibulin, P. V. Pikhitsa, H. Jiang, and E. I. Kauppinen, *Carbon* 43, 2251 (2005).
25. A. Moisala, A. G. Nasibulin, S. D. Shandakov, H. Jiang, and E. I. Kauppinen, *Carbon* 43, 2066 (2005).
26. A. Moisala, A. G. Nasibulin, D. P. Brown, H. Jiang, L. Khriachtchev, and E. I. Kauppinen, *Chem. Engg. Sci.* 61, 4393 (2006).
27. K. Hata, D. N. Futaba, K. Minuzo, T. Namai, M. Yumura, and S. Iijima, *Science* 306, 1362 (2004).
28. M. Audier, M. Coulon, and L. Bonnetain, *Carbon* 21, 93 (1983).
29. M. J. Bronikowski, P. A. Willis, D. T. Colberg, K. A. Smith, and R. E. Smalley, *J. Vac. Sci. Technol. A* 19, 1800 (2001).
30. A. Moisala, A. G. Nasibulin, and E. I. Kauppinen, *J. Physics: Cond. Matt.* 15, 3011 (2003).
31. Z. Zhao, L. Ci, L. Song, L. Yan, D. Liu, H. Yuan, Y. Gao, J. Wang, L. Liu, W. Zhao, G. Wang, and S. Xie, *Carbon* 41, 2607 (2003).
32. B. Zheng, C. Lu, G. Gu, A. Makarovski, G. Finkelstein, and J. Liu, *Nano Lett.* 2, 895 (2002).

Received: 17 December 2007. Revised/Accepted: 20 March 2008.